Journal of Energy Chemistry 80 (2023) 247–255

Contents lists available at ScienceDirect

Journal of Energy Chemistry

journal homepage: www.elsevier.com/locate/jechem

http://www.journals.elsevier.com/journal-of-energy-chemistry/

Electronically modulated *d*-band centers of MOF-derived carbon-supported Ru/HfO_2 for oxygen reduction and aqueous/flexible zinc-air batteries

Chuan Hu [a,1], Fengli Wei [a,1], Qinrui Liang [a], Qiming Peng [a], Yuting Yang [a], Tayirjan Taylor Isimjan [b], Xiulin Yang [a,*]

[a] Guangxi Key Laboratory of Low Carbon Energy Materials, School of Chemistry and Pharmaceutical Sciences, Guangxi Normal University, Guilin 541004, Guangxi, China
[b] Saudi Basic Industries Corporation (SABIC) at King Abdullah University of Science and Technology (KAUST), Thuwal 23955-6900, Saudi Arabia

ARTICLE INFO

Article history:
Received 29 December 2022
Revised 28 January 2023
Accepted 30 January 2023
Available online 11 February 2023

Keywords:
Ru/HfO_2
Charge interaction
Oxygen vacancy
Oxygen reduction
Zinc-air battery

ABSTRACT

The construction of oxide/metal composite catalysts is a competent means of exploiting the electronic interactions between oxide/metal to enhance catalytic activity. In this work, we construct a novel heterogeneous composite (Ru/HfO_2-NC) with Ru/HfO_2 nanoparticles nested in nitrogen-doped porous carbon via a zeolitic imidazole frameworks-assisted (ZIF) co-precipitation and calcination approach. In particular, ZIF guides an in-situ construction of nested configuration and confines the scattered nanoparticles. Strikingly, Ru/HfO_2-NC exhibits unusual ORR activity, superb durability, and methanol tolerance in 0.1 M KOH solution with high half-wave potential ($E_{1/2}$) of 0.83 V and follows a near-4e$^-$ reaction pathway. Additionally, the ZAB assembled with cathodic Ru/HfO_2-NC outputs a power density of 157.3 mW cm^{-2}, a specific capacity of 775 mA h g_{Zn}^{-1}, and a prolonged lifespan of 258 h at 5 mA cm^{-2}. Meanwhile, the catalyst has demonstrated potential applicability in flexible ZAB. As suggested by experimental results and density functional theory (DFT) analysis, the remarkable property possibly originated from the optimization of the adsorption and desorption of reactive intermediates caused by the reconfiguration of the electronic structure between Ru and HfO_2.

1. Introduction

Renewable energy development is a practical action in response to the current environment-friendly energy strategy [1]. As an energy conversion device with a theoretical energy density (1086 Wh kg^{-1}) several times higher than Li-ion batteries, the zinc-air battery has received increasing attention [2]. The performance of the entire zinc-air battery is dominated by the oxygen reduction reaction that occurred on the air cathode [3,4]. In alkaline electrolytes, the reduction of oxygen molecules to OH^- requires a complex 4-electron pathway, which is a pivotal guarantee for high-efficiency ORR and superior reliability [5,6]. Nevertheless, the sluggish kinetics, complex reduction route, and high energy intermediates limit efficient ORR catalysis, which impedes the extensive implementation [7,8]. Yet, platinum group metal (PGM) catalysts (such as commercial Pt/C and Pt-based alloy) still occupy the benchmark position in the ORR catalysts [9]. However, their low abundance, inferior stability, and intolerance to methanol limit large-scale applications [10,11]. Therefore, designing low-cost metal-based electrocatalysts with excellent activity and durability is essential for the development of zinc–air batteries.

As a result, the formation of mixed oxides with lower-cost noble metals (Ru, Os, Rh) and inexpensive transition metals (Fe, Co, Ni, and Zn) are the two approaches to decreasing the cost while not compromising performance [12]. The early transition metals (Hf, Zr, Ti) have been explored as modifiers, which have excellent stability in the broader pH range, for instance, Zr-based catalysts have shown superior ORR performance [13,14]. Hf as a type of metal with more abundant reserves and lower price than Ru and Ir, the Hf-based catalysts, nevertheless, have attracted fewer explorations. Peculiarly, Hf-based and Zr-based materials have the similar chemical and physical properties [15]. Mitsuharu Chisaka et al. demonstrated a novel carbon-supported hafnium oxynitride nanoparticles (HfO_xN_y-C) [16]. Monoclinic hafnium oxide nanoparticles with oxygen defects were confirmed to perform ORR activity in acidic solutions for the first time. In contrast, it requires multiple

* Corresponding author.
E-mail address: xlyang@gxnu.edu.cn (X. Yang).
[1] These authors contribute equally to this work.

https://doi.org/10.1016/j.jechem.2023.01.047

calcination under H_2 or NH_3 atmospheres at high temperatures. Later, the same team hydrothermally synthesized hafnium oxide nanoparticles on reduced graphene oxide flakes [17]. The flakes coated the HfO_x catalyst with a carbon layer to increase conductivity and the number of active sites. Mayilvel Dinesh Meganathan et al. reported a novel hafnium phosphide-reduced graphene oxide nanosheets (HfP-rGO NS) and hafnium disulfide-reduced graphene oxide nanosheets (HfS_2-rGO NS) [18]. The rGO sheets overcame the low conductivity of Hf and created a synergistic effect to promote ORR performance. Nevertheless, both approaches require multistep synthesis under harsh environments that hinder their practical application. Furthermore, shaping and thermally controlling the catalyst morphology and crystal structure is often challenging under the harsh environment that profoundly affects the arrangement of the active sites at the atomic level and surface configuration, thereby influencing the catalytic performance and stability [19]. Therefore, it is of great practical significance to develop a Hf-based catalyst with a simple synthesis process and excellent performance. Ruthenium-based catalysts have drawn considerable attention due to their lower cost compared to Pt but their excellent activity in hydrogen/oxygen evolution reactions (HER/OER) and oxygen reduction reactions (ORR) [20]. In addition, the electronic property of Ru is similar to Pt, which can regulate the adsorption energy of intermediate species in the ORR/OER processes and lower the reaction energy barrier, thus improving the reaction kinetics [21]. Wei et al. found that Ru doping can profitably modulate the surface electronic structure and active sites of cobalt oxide [22], thereby enhancing the reaction's kinetics [23]. Therefore, a unique synergy between Ru and HfO_2 is anticipated to improve ORR activity. Furthermore, carbon-based composites prepared by MOF derivatization supply conductive and porous support for the Ru/HfO_2 [24].

In this work, zeolitic imidazole framework-8 (ZIF-8) was employed to guide the synthesis of a novel nitrogen-doped porous carbon nested Ru/HfO_2 nanoparticles heterogeneous composite where ZIF-8 promoted versatile surface geometry, high specific surface area, multiple pores, and N species [25]. The Hf doped ZIF-8 (Hf-ZIF-8) was prepared through a host–guest method to achieve the easy capture and uniform dispersion of Hf^{4+}. Ru is further loaded on Hf-ZIF-8 to increase more active species and induce charge interaction. This ZIF confinement effect facilitates the formation of scattered Ru and HfO_2 nanoparticles during calcination. Calcination transformed the ZIF-8 framework into a graphitized nitrogen-doped carbon scaffold. It established the nanoparticles and carbon embedded structure, thereby improving the stability and electrical conductivity of the nanoparticles. Benefiting from the open frame structure of ZIF-8, the as-prepared catalyst possesses large specific surface and abundant mesopores. Additionally, the presence of oxygen vacancies can increase the electrochemically active sites and accelerate the adsorption of oxygenates. Density functional theory (DFT) calculations have demonstrated that Ru composite with HfO_2 can significantly modulate the *d*-band center of the material, producing moderate binding for oxygen intermediates such as *OOH and *OH, and thus enhancing catalytic activity. Moreover, we explored the potential applications of the catalyst for aqueous and flexible ZAB.

2. Experimental

2.1. Materials

Zinc nitrate hyexahdrate ($Zn(NO_3)_2{\cdot}6H_2O$, 99%) was purchased from Sinopharm Chemical Reagent Co., ltd. 2-Methylimidazole (98 %) was purchased from Shanghai Aladdin Biochemical Technology Co., ltd. Methanol (CH_3OH, 99.5 %) was purchased from Xilong Chemical Co., ltd. Ruthenium trichloride ($RuCl_3{\cdot}xH_2O$, 99 %, Ru: 37–40 wt%) was purchased from Beijing Enokai Technology Co., ltd. Hafnium chloride ($HfCl_4$, AR, 99.5 %) was purchased from Shanghai Maclean Biochemistry Co., ltd. And commercial Pt/C (20 wt% Pt) was purchased from Shanghai Maclean Biochemistry Co., ltd. All reagents were analytical grade and were used directly without further purification.

2.2. Synthesis of ZIF-8 and Hf-ZIF-8

The ZIF-8 was first synthesized according to the previous approach [26]. In a typical synthesis, a 50 mL methanol solution containing 2-methylimidazole (1.630 g) was added to another 50 mL methanol solution containing $Zn(NO_3)_2{\cdot}6H_2O$ (0.735 g). Then, the mixed solution was stirred for 12 h under ambient temperature. The sample was then collected by centrifugation, washed with methanol several times, and dried at 60 °C overnight. The Hf-ZIF-8 was developed by the same procedure except additionally adding 60 mg $HfCl_4$ into the zinc salt solution. The sample was denoted as Hf-ZIF-8.

2.3. Synthesis of NC and HfO_2-NC

The ZIF-8 and Hf-ZIF-8 powers were heated to 950 °C at a rate of 5 °C/min and maintained for 2 h in a nitrogen atmosphere, respectively. The corresponding products were separately designated as NC and HfO_2-NC.

2.4. Synthesis of Ru/Hf-ZIF-8 and Ru-ZIF-8

200 mg Hf-ZIF-8 and ZIF-8 was suspended in 40 mL methanol solution and sonicated for 15 min, respectively. Then 15 mg $RuCl_3{\cdot}xH_2O$ was added and stirred for 24 h. And the products were obtained by centrifugation, wishing with ethanol three times and drying at 60 °C overnight. The corresponding products were labeled as Ru/Hf-ZIF-8 and Ru-ZIF-8, respectively. In a contrast, changed the amount of $RuCl_3{\cdot}xH_2O$ that was added into Hf-ZIF-8 to 10 and 20 mg but keep the other steps no changed. And then marked as Ru_{10}/Hf-ZIF-8 and Ru_{20}/Hf-ZIF-8, respectively.

2.5. Synthesis of Ru-NC and Ru/HfO_2-NC

A certain amount of Ru-ZIF-8 and Ru/Hf-ZIF-8 powers were heated to 950 °C at a rate of 5 °C/min and maintained for 2 h in nitrogen atmosphere respectively. The obtained samples were separately noted as Ru-NC, Ru/HfO_2-NC. In a contrast, Ru_{10}/Hf-ZIF-8 and Ru_{20}/Hf-ZIF-8 were calcined under the same condition, and the obtained products were marked as Ru_{10}/HfO_2-NC and Ru_{20}/HfO_2-NC, respectively.

3. Results and discussions

3.1. Structure characterization

As shown in Fig. 1(a), Ru/HfO_2-NC was synthesized via co-precipitation, adsorption, and high-temperature calcination. The adoption of MOF-assisted approach was to construct the carbon support in-situ. Firstly, a methanol solution of 2-methylimidazole (2-MeIM) was added into a methanol solution containing Zn^{2+} and Hf^{4+}, the Zn^{2+} coordinated with the 2-MeIM and co-precipitated to form Hf doped ZIF-8 (Hf-ZIF-8) in ambient temperature. Secondly, the prepared Hf-ZIF-8 was added into a methanol solution by ultrasonic treatment to form a uniform suspension, then a certain amount of $RuCl_3$ was added, and under stirring, Hf-ZIF-8 adsorbed Ru^{3+} adequately to form Ru doped Hf-ZIF-8

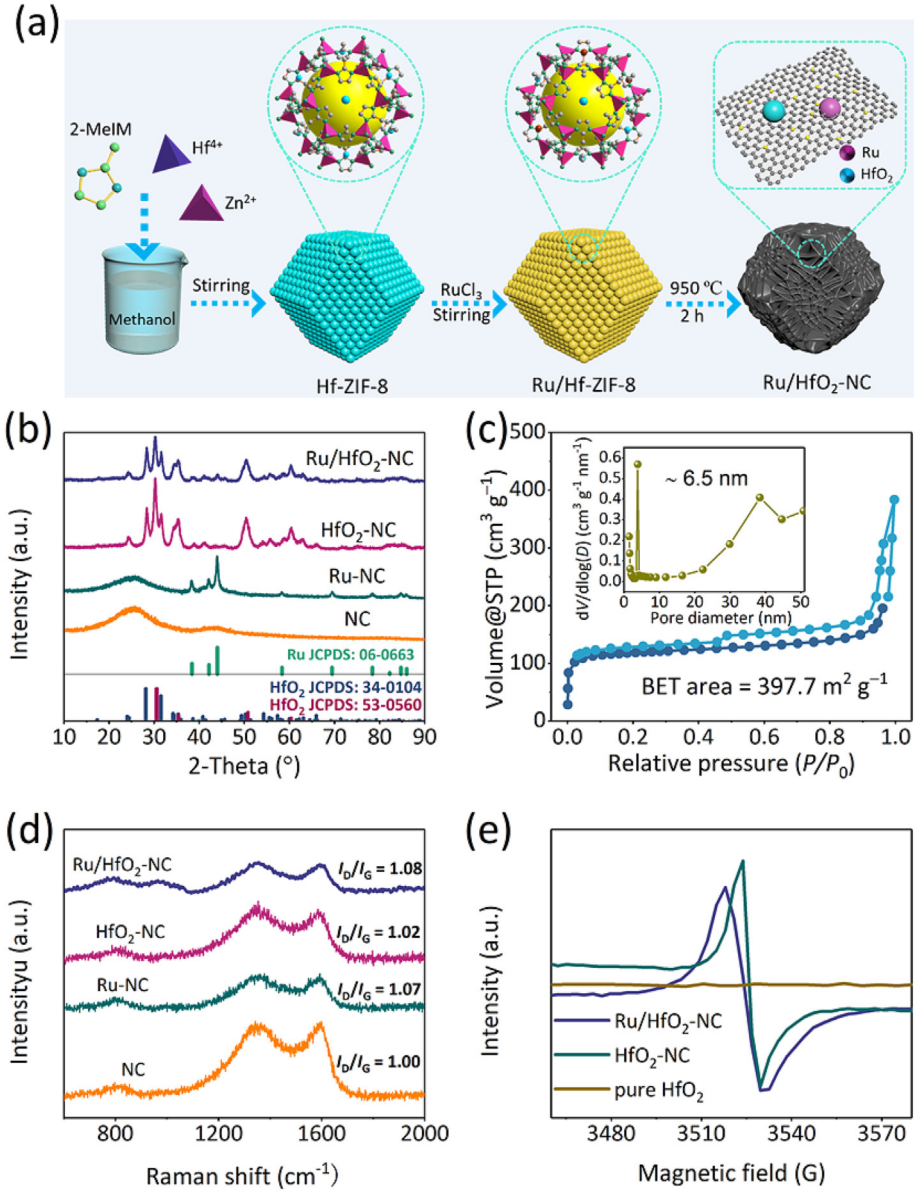

Fig. 1. (a) The synthesis schematic diagram of Ru/HfO_2-NC. (b) XRD patterns of the as-prepared catalysts. (c) N_2 adsorption–desorption isotherm of Ru/HfO_2-NC (inset: corresponding pore size distribution curve). (d) Raman spectra of the as-prepared catalysts. (e) EPR spectra of Ru/HfO_2-NC, HfO_2-NC, and pure HfO_2.

(Ru/Hf-ZIF-8). Lastly, the Ru/Hf-ZIF-8 powder was calcined at 950 °C under N_2 atmosphere and in-situ constructed a heterogeneous composite catalyst of Ru/HfO_2 nanoparticles embedded in N-doped porous carbon (Ru/HfO_2-NC). This approach provided a support for Ru/HfO_2 while achieving a strong binding of the metal particles to the carbon support. In addition, the metal contents of the different catalysts were determined by inductively coupled plasma atomic emission spectroscopy (ICP-AES) measurement (Table S1), and the mass content of Ru in the optimal catalyst was about 2.35 %.

X-ray diffraction (XRD) was carried out to analyze the phase structures of the synthesized samples. As shown in Fig. S1(a), the XRD patterns of prepared ZIF-8 and Ru/Hf doped ZIF-8 were consistent with that of simulated ZIF-8, indicating the ZIF-8 was synthesized successfully, and Hf/Ru had no effect on the crystal phase of ZIF-8. Fig. 1(b) presented the XRD patterns of the calcined samples. NC exhibited two broad "humps" at around 25° and 44°, assigning to the (002) and (101) planes of graphitic carbon [27]. In Ru-NC, distinct characteristic peaks of hexagonal Ru (JCPDS: 06–0663) appeared. Two types of characteristic peaks of HfO_2 existed in HfO-NC, monoclinic (JCPDS: 34–0104) and cubic (JCPDS: 53–0560) HfO_2, respectively. Ru/HfO-NC displayed the same characteristic peaks of HfO_2 with HfO_2-NC and the identical distinct peaks of hexagonal Ru with Ru-NC. Moreover, the contrast samples with different amounts of $RuCl_3$ displayed almost identical characteristic peaks with Ru/HfO_2-NC (Fig. S1b). The specific surface area and pore property of Ru/HfO_2-NC was analyzed by Brunauer–Emmett–Teller (BET) analytical technique. In Fig. 1(c), the N_2 adsorption–desorption isotherms revealed a typical type IV curve with H_2-type hysteresis loop, confirming the presence of mesopores [12]. The measured BET surface area was 397.7 m^2 g^{-1}, and the calculated average pore size by Barrett–Joyner–Halenda (BJH) model was around 6.5 nm, proving the dominate existence of mesopore [28]. While the specific surface area of NC reached 1125.3 m^2 g^{-1}, and the average pore size was around 1.72 nm (Fig. S2). The addition of Ru and HfO_2 significantly decreased the specific surface area of Ru/HfO_2-NC but increased its average pore size. A prosperous mesopore was beneficial for exposing more active sites and

improving mass transfer [29]. The resultant catalysts emerged two peaks in Raman spectra, where the D-band (disordered graphitic structures) at 1340 cm^{-1} and the G-band (vibration of the sp^2 hybridized carbon) at 1581 cm^{-1} [30]. The intensity ratios (I_D/I_G) of NC, Ru-NC, HfO_2-NC, and Ru/HfO_2-NC were calculated to be 1.00, 1.07, 1.02, and 1.08 (Fig. 1d). The highest I_D/I_G ratio indicated the more carbon structural defects for Ru/HfO_2-NC, which effectively increased the adsorption of oxygen [31]. Besides, the Raman peak at around 800 cm^{-1} was attributed to the vibration of the C — C bond [32]. Electron paramagnetic resonance (EPR) measurement first detected the oxygen vacancies. As shown in Fig. 1(e), the EPR spectra of Ru/HfO_2-NC and HfO_2-NC exhibited a strong signal at g = 1.999 and 1.995 [33], where the apparent peak shift was affected by the binding forces of surrounding atoms [34,35]. The results indicated the presence of unpaired electrons caused by oxygen vacancies, which can improve conductivity and surface catalysis [36]. The oxygen vacancies originated from HfO_2 lattice and could be confirmed by high resolution transmission electron microscope (HR-TEM) images (Fig. S3).

The morphology of resultant samples was identified by scanning electron microscope (SEM) and transmission electron microscopy (TEM). As depicted in Fig. S4(a), the prepared Hf-ZIF-8 presented a morphology of rhombic dodecahedron. The morphology of Ru/Hf-ZIF-8 was changed slightly (Fig. S4b) when Ru^{3+} was introduced due to the deprotonation of 2-MeIM linkers and broader growth directions during the regrowth of Hf-ZIF-8 [37]. After calcination, Ru/HfO_2-NC showed a morphology of stalactite-like irregular three-dimensional structure with raised surface (Fig. 2a). TEM image of Ru/HfO_2-NC observed the presence of cavities (Fig. 2b). The high-resolution transmission electron microscopy (HR-TEM) images in Fig. 2(c-e) revealed three species of interplanar spacings of 0.315, 0.255 and 0.206 nm, assigning to the (-111) plane of monoclinic HfO_2, the (002) plane of cubic HfO_2, and the (101) plane of hexagonal Ru, respectively. The clear interfaces between metal and carbon support in the HR-TEM images indicated the successful construction of the embedded structure. As depicted in Fig. 2(f), the diffraction rings in the area electron diffraction (SAED) pattern revealed the characteristic planes of monoclinic HfO_2 and Ru. Energy dispersive X-ray spectroscopy (EDS) detected the signals of C, N, O, Ru, and Hf (Fig. S5). High angle annular dark field transmission electron microscope (HAADF-TEM) image and the corresponding elemental mapping images revealed that the C, N, O, Ru, and Hf elements were evenly distributed in entire structure. We failed to observe a clear lattice interface according to the test results. However, we could see the coexistence of Ru and HfO_2 in the same region by high-resolution transmission electron images. In addition, the selected area electron diffraction pattern also proved this feature and the element mapping images demonstrate the overlapping distribution of elements Ru and HfO_2. We assumed that Ru and HfO_2 are successfully composited based on the above results.

High-resolution X-ray photoelectron spectroscopy (XPS) was used to investigate the surface elemental composition and chemical states of these catalysts. The XPS survey spectra of different catalysts were presented in Fig. S6. Fig. 3 depicted the high-resolution C 1*s* + Ru 3*d*, Hf 4*f* and O 1*s*. In detail, Ru/HfO_2-NC and HfO_2-NC both showed four deconvoluted peaks in high-resolution C 1*s* spectra, which belong to C=C (284.00 eV), C—C (284.80 eV), C—O/C—N (286.00 eV), and C=O (288.70 eV) [38]. The high-resolution Ru 3*d* spectra of Ru/HfO_2-NC were deconvoluted into two peaks at 279.56 and 280.33 eV, attributing to Ru^0 $3d_{5/2}$ and RuO_2 $3d_{5/2}$ (Fig. 3a) [39]. Besides, the Ru 3*p* XPS spectrum was presented in Fig. S7. The RuO_2 possibly originated from exposure of the sample to air [40]. A trace amount of RuO_2 was found on the surface by XPS. However, high-resolution transmission electron microscopy images and selected area electron diffraction images only revealed lattice stripes and electron diffraction rings of metallic Ru, indicating Ru mainly in metallic form. Three characteristic peaks appeared at 398.12,

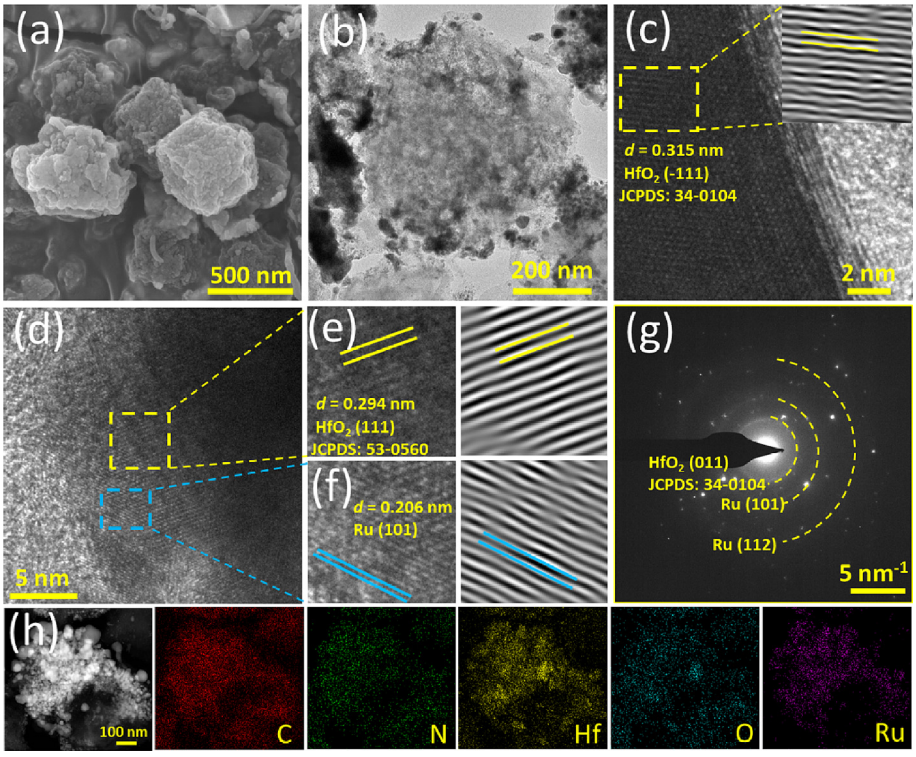

Fig. 2. (a) SEM image, (b) TEM image, (c-f) HR-TEM images and corresponding inverse fast Fourier transformation images, (g) SAED image, and (h) HAADF-TEM and EDS mapping images of Ru/HfO_2-NC.

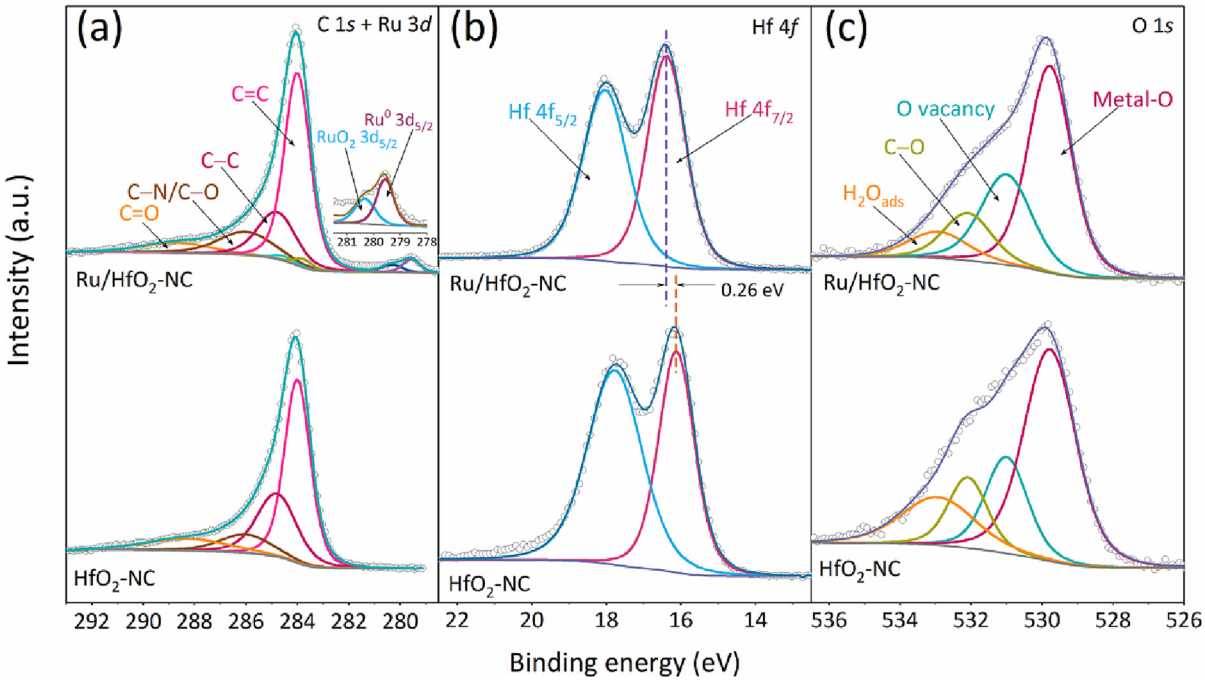

Fig. 3. High-resolution (a) C 1*s* + Ru 3*d*, (b) Hf 4*f*, and (c) O 1*s* XPS spectra of as-prepared catalysts.

400.18, and 402.11 eV in the high-resolution N 1*s* spectra of different catalysts (Fig. S8), attributing to pyridinic-N, pyrrolic-N, and graphitic-N, respectively [41]. Ru/HfO_2-NC and HfO_2-NC all exhibited clear doublets for Hf $4f_{7/2}$ and Hf $4f_{5/2}$ sublevels in Hf 4*f* spectra, indicating the presence of fully oxidized HfO_2 [19]. For Ru/HfO_2-NC, Hf $4f_{7/2}$ and Hf $4f_{5/2}$ deconvoluted peaks were located at 16.38 and 17.90 eV [15]. Deconvoluted Hf $4f_{7/2}$ and Hf $4f_{5/2}$ peaks of HfO_2-NC were centered at 16.12 and 17.77 eV (Fig. 3b). Notably, Ru/HfO_2-NC presented an upshift of 0.26 eV of Hf 4*f* orbital binding energy compared to HfO_2-NC, suggesting a charge transfer from HfO_2 to other components existed in Ru/HfO_2-NC. The O 1*s* spectra of Ru/HfO_2-NC and HfO_2-NC were deconvoluted into four peaks at 529.79, 531.05, 532.14 and 533.10 eV, corresponding to metal-O, oxygen vacancy, C—O and H_2O_{ads}, respectively (Fig. 3c) [42]. Accurately, the XPS signal of oxygen vacancy should be attributed to the surface hydroxyl groups that are formed by the adsorption and dissociation of water by the oxygen vacancy sites, rather than the missing oxygen [43].

3.2. Electrochemical evaluation for ORR

Rotating disk electrode (RDE) and rotating ring disk electrode (RRDE) were used to assess the ORR performance of these catalysts in an O_2/N_2-saturated 0.1 M KOH solution. The effects of the $RuCl_3$ loading and Ru/HfO_2 ratio on the catalytic activity were investigated. As shown in Fig. S9(a and b), Ru/HfO_2-NC possessed the most positive reduction peak, the highest half-wave potential ($E_{1/2}$) and maximum limiting current density (J_L), indicating the highest activity. Therefore, Ru/HfO_2-NC is the target catalyst for the following discussion. The ORR activity of these catalysts was initially assessed by cyclic voltammetry (CV) curves. In Fig. 4 (a), all components except NC showed significant cathodic reduction peaks, indicating that the activity was more efficient in the presence of metallic species. Further linear sweep voltammetry (LSV) tests elucidated the performance differences of individual catalysts. As shown in Fig. 4(b) and Table S2, Ru/HfO_2-NC exhibited a maximum J_L (4.92 mA cm^{-2}) as compared to Pt/C (5.27 mA cm^{-2}), HfO_2-NC (4.17 mA cm^{-2}), Ru-NC (3.80 mA cm^{-2}), and NC (3.52 mA cm^{-2}). The $E_{1/2}$ of Ru/HfO_2-NC (0.83 V) was higher than that of HfO_2-NC (0.78 V) and Ru-NC (0.81 V). The precious metal mass activity of Ru/HfO_2-NC, Ru-NC and Pt/C were 0.31, 0.20 and 0.39 mA μg^{-1} respectively (Fig. S10). The result demonstrated that the combination of Ru and HfO_2 could dramatically improve catalytic performance, which may be the result of charge interactions between these components. Trace amounts of single-atom Ru sites probably formed during the preparation of the catalysts, while the KSCN poisoning experiment implied they contributed little to the overall catalytic activity (Fig. S11). Additionally, all of the prepared catalysts exhibited inferior OER activity (Fig. S12). Next, we calculated the kinetic current density (J_K) from the Koutecky – Levich (K – L) equation for each catalyst to illustrate the difference in their performance, as shown in Fig. S13. The J_K is a function of overpotential (η) [44], Ru/HfO_2-NC presented a larger J_K compared to Ru-NC and HfO_2-NC, indicating its faster reaction kinetics. Furthermore, in an effort to analyze the performance advantages of Ru/HfO_2-NC in more depth, calculations of reaction electron transfer number (n) and hydrogen peroxide yields were carried out subsequently. The n is a descriptor clarifying catalytic mechanism [12]. Here, LSV curves of these catalysts were recorded by RDE at various rotate speeds (400–2500 rpm) to estimate n. The LSV curves of Ru/HfO_2-NC were displayed in Fig. 4(c), and further fitting it by K – L equation obtained the fit plots (Fig. 4d). The K – L plots showed excellent linearity from 0.3 to 0.4 V, revealing the first-order reaction for dissolved O_2 of Ru/HfO_2-NC for ORR [45]. The calculated n (3.98) was close to 4, implying a four-electron pathway from O_2 to OH^-. In comparison, n for NC, Ru-NC, and HfO_2-NC were calculated to be 2.59, 3.74, and 3.49, respectively (Fig. S14), indicating a lower selectivity for four-electron pathway. RRDE measurement is a direct mean to further verify the ORR pathway by monitoring the intermediate peroxide species. As presented in Fig. 4(e), Ru/HfO_2-NC occurred a H_2O_2 yield of 1.56 %-12.01 % from 0.2 to 0.8 V (vs RHE), with n ranging from 3.76 to 3.97, certifying its ORR process followed a high selectivity of OH^- as the main product [46]. While NC, HfO_2-NC, and Ru-NC exhibited a much higher H_2O_2 yield and a smaller n, verifying their inferior selectivity for four-electron pathway. In comparison, the RRDE test was a direct measurement of

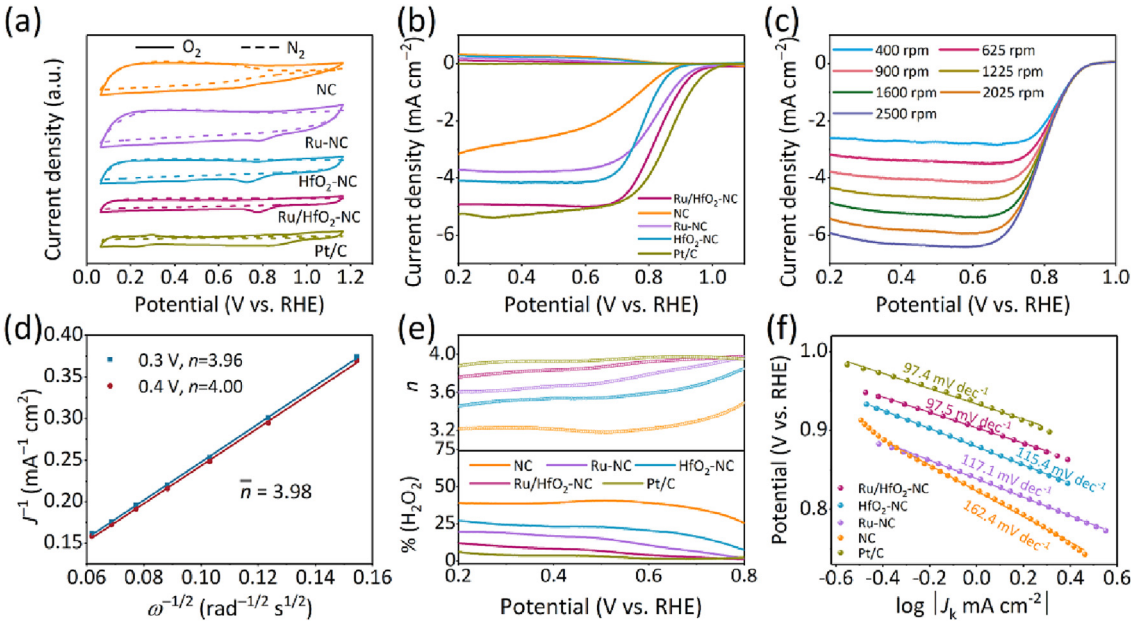

Fig. 4. (a) CV curves of different catalysts. (b) ORR polarization curves of different catalysts. (c) ORR polarization curves of Ru/HfO_2-NC at various rotations. (d) Koutecky – Levich (K – L) plots of Ru/HfO_2-NC. (e) The H_2O_2 yield (%) and electron transfer numbers (n) of different catalysts. (f) Tafel plots of different catalysts abstracted from LSV curves. All tests were conducted in 0.1 M KOH solution.

the peroxide yield to derive the electron transfer number, which was relatively more accurate than the RDE test. Therefore, we determined the reaction-electron-transfer-number mainly by the RRDE test, and the RDE test result was used as a reference. The Tafel slopes of these catalysts were calculated to determine the reaction kinetics (Fig. 4f) [47]. Among all catalysts, Ru/HfO_2-NC gave a smaller Tafel slops (97.5 mV dec^{-1}) with respect to NC (162.4 mV dec^{-1}), HfO_2-NC (115.4 mV dec^{-1}), Ru-NC (117.1 mV dec^{-1}), and Pt/C (97.4 mV dec^{-1}), demonstrating its favorable reaction kinetics [48].

Double-layer capacitance (C_{dl}) and electrochemical surface areas (ECSA) were measured to estimate the effective contact area between electrolyte and catalyst. The C_{dl} value of Ru/HfO_2-NC was 25.5 mF cm^{-2}, lowing than that of Ru-NC (77.1 mF cm^{-2}), NC (62.6 mF cm^{-2}), and HfO_2-NC (54.3 mF cm^{-2}) (Fig. S15 and Fig. S16). This phenomenon could be explained by the partial occupation of the pores on the carbon matrix by the metal species, and the relatively large amount of metal particles would increase the compactness of the material. Furthermore, the ECSA values of these catalysts were measured by $K_3[Fe(CN)_6]$ experiment (Fig. S17a-c). As shown in Fig. S17(d), the ECSA values of Ru/HfO_2-NC, Ru-NC, and NC calculated from the fitting plots according to the Randles-Sevcik equation were 0.42, 0.64, and 0.59 cm^2, respectively [49]. Ru/HfO_2-NC exhibited the lowest C_{dl} and ECSA, contrary to its surpassing performance. The results manifested that the intrinsic advantage of the active sites could diminish the disadvantages caused by lower ECSA and C_{dl}. To corroborate this point, we normalized the J_K by ECSA (Fig. S18). The dedication of ECSA per square centimeter to J_K was much greater in Ru/HfO_2-NC than in Ru-NC and HfO_2-NC, demonstrating that the intrinsic activity of the active sites, rather than the number of active sites, was responsible for the difference in their activities [50]. This further proved that the interaction between Ru and HfO_2 can enhance the intrinsic activity of active sites. Methanol cross-resistance and durability were key criteria for the assessment of electrocatalysts, which were assessed by chronoamperometry measurement, respectively. As shown in Fig. S19, the current density of Ru/HfO_2-NC changed negligibly after the injection of 3 M methanol whereas Pt/C decreased sharply, clearly demonstrating Ru/HfO_2-NC had the superior methanol tolerance performance than Pt/C. At constant potential, a small decay (4.3 %) of current density was obtained for Ru/HfO_2-NC after 10 h, which was visibly lower than that of Pt/C (22.5 %) (Fig. S20), confirming the excellent durability of Ru/HfO_2-NC.

The SEM, TEM and XPS characterizations after stability were employed to investigate the morphological and structural changes of the catalyst. As shown in Fig. S21a and b), the SEM and TEM images demonstrated a substantially maintained morphology of the catalyst after the stability test. The EDS spectrum revealed the presence of C, N, Hf, O and Ru (Fig. S21c). In addition, the element mapping images indicated their uniform distribution throughout the catalyst (Fig. S21d). The XPS full spectrum showed the signals of C, N, O, Hf and Ru in the catalyst, while F originated from the Nafion solution in the catalyst ink (Fig. S22a). The fitted high-resolution C 1*s* + Ru 3*d* spectra indicated the bonding of C=C, C—C, C—O/C—N and C=O bonding species [51], while the signal for K is attributed to KOH in solution (Fig. S22b). Besides, the fitted peaks at 279.53 and 283.73 eV were attributed to Ru $3d_{5/2}$ and Ru $3d_{3/2}$ [52]. The high-resolution Hf 4*f* spectra showed one distinct doublet representing HfO_2. In contrast, the insignificant doublet at lower binding energies was attributed to metal Hf 4*f* orbitals, which may be due to the long-term exposure of HfO_2 to the reduction potential (Fig. S22c). The peak at the higher binding energy was probably associated with $Hf(OH)_4$ [17]. Moreover, the fitted high-resolution O 1*s* spectra revealed the existence of metal-O and O vacancy. In comparison, the fitted peaks in the high-resolution N 1*s* spectra were attributed to pyridinic-N, pyrrolic-N, and graphitic-N [53], respectively (Fig. S22d and e).

3.3. Density functional theory (DFT) calculation

Density functional theory (DFT) calculation was carried out to gain insight into the origin of the enhanced ORR catalytic activity of Ru/HfO_2-NC. The optimized model structures of the pristine Ru/HfO_2, Ru and HfO_2 were provided in Fig. S23. An ORR process generally involves four intermediate species, *i.e.* surface-adsorbed O_2*, OOH*, O*, and OH* [54]. Fig. 5(a) depicted the optimal struc-

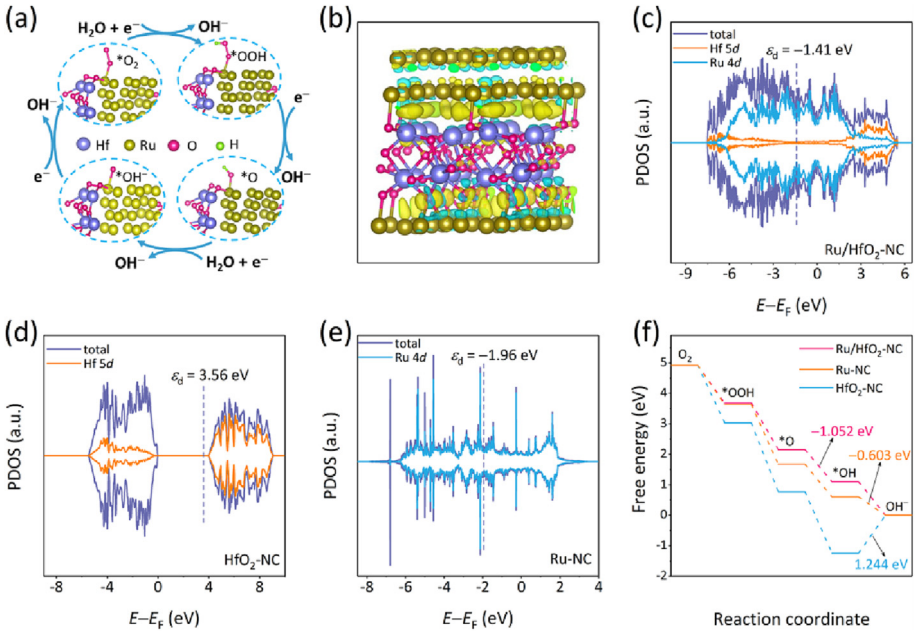

Fig. 5. (a) ORR mechanism on Ru/HfO_2-NC. (b) The charge density difference for Ru/HfO_2-NC, the yellow and blue regions represent electron accumulation and depletion, respectively. Density of states of (c) Ru/HfO_2-NC, (d) HfO_2-NC, and (e) Ru –NC. (f) Gibbs free energy diagram for ORR on Ru/HfO_2-NC, HfO_2-NC, and Ru –NC (U = 0 V).

ture models for the adsorption of four intermediates by Ru/HfO_2-NC and the catalytic mechanism process. The optimal structure models demonstrated that Ru site in Ru/HfO_2-NC was thermodynamically desirable for adsorbing intermediates. The charge density differences were theoretically analyzed to investigate further the electronic structure characteristics of Ru/HfO_2-NC, which indicated that significant charge accumulation occurred at the interfaces between Ru and HfO_2 (Fig. 5b). The results suggested that the interaction between Ru and HfO_2 can modulate the interface electronic structure between them, thereby optimizing the adsorption and desorption of reaction intermediates [55]. Additionally, we performed a projected density of states (*p*DOS) calculation analysis for Ru/HfO_2-NC, HfO_2-NC and Ru-NC (Fig. 5c-e). Obviously, HfO_2-NC exhibited a broad band gap in up and down spin state at the Fermi energy level (E_f), revealing its semiconductor property with low electrical conductivity [56]. When constructed as a composite with Ru, Hf 5*d* orbit in Ru/HfO_2-NC produced a continuous DOS at E_f, indicating an improvement in its electron transfer capacity, which suggested a strong electron structure synergy between Ru and HfO_2. The calculated *d*-band center of Ru/HfO_2-NC, HfO_2-NC, and Ru-NC were – 1.41, 3.56, and – 1.96 eV, respectively. The moderate *d*-band center of Ru/HfO_2-NC effectively regulated the balance between adsorption and desorption of the reaction intermediates, thus improving the catalytic activity [57]. As shown in Fig. 5(f) and Table S4, all steps were downhill and exothermic for Ru/HfO_2-NC and Ru-NC, whereas the first three reaction steps were downhill and exothermic and the last step was uphill and endothermic for HfO_2-NC. Concerning Ru/HfO_2-NC and Ru-NC, the minimum negative Gibbs free energy change (ΔG) suggested a sluggish rate-determining step. Therefore, the thermodynamic rate-determining step (RDS) for Ru/HfO_2-NC formed the intermediate *OH, while Ru-NC was the formation of OH^-. Gibbs free energy calculations revealed that Ru/HfO_2-NC exhibited the most negative free energy change of – 1.052 eV in RDS at 0 V compared to – 0.603 eV of Ru-NC. But, for HfO_2-NC, the positive ΔG change revealed a sluggish rate-determining step, in which the OH^- formation ΔG was calculated to be 1.244 eV. Consequently, in comparison to the higher barrier of the rate-determining step of Ru-NC and HfO_2-NC, Ru/HfO_2-NC was kinetically and thermodynamically more desirably active for reaction intermediates. To better understand this conclusion, we calculated the oxygen adsorption energy of different catalysts (Fig. S24). Usually, moderate oxygen adsorption energy can balance the formation and desorption of intermediates in the subsequent process [12]. The calculated oxygen adsorption energies for Ru/HfO_2-NC, Ru-NC and HfO_2-NC, were – 0.416, – 0.616 and – 1.60 eV, respectively. The smaller oxygen adsorption energy of Ru/HfO_2-NC implied a less intense oxygen adsorption property, which may modulate the adsorption and desorption of intermediates during subsequent reactions. While strong oxygen adsorption of HfO_2-NC and Ru-NC may lead to an unfavourable OH^- desorption or even a more significant generation energy barrier. The ΔG change of the RDS in Ru/HfO_2-NC was – 1.052 eV, corresponding to a 0.178 V theoretical overpotential, while Ru-NC is 0.627 V. Therefore, a lower overpotential indicated better electrochemical performance.

3.4. Zinc-air battery test

The practical performance of Ru/HfO_2-NC was evaluated by an aqueous ZAB device, as illustrated in Fig. 6(a) for the schematic diagram of ZAB. The as-prepared catalyst was fixed on hydrophobic carbon paper as air cathode, a zinc foil acted as anode, and assembled with the electrolyte containing 6 M KOH and 0.2 M $Zn(Ac)_2$. The Ru/HfO_2-NC-based battery exhibited a higher open-circuit voltage (OCV) of 1.54 V than Pt/C-based battery (1.43 V) (Fig. 6b). And the specific capacity of Ru/HfO_2-NC was 775.0 mA h g_{Zn}^{-1} at a discharge density of 10 mA cm^{-2}, whereas the Pt/C was 700.8 mA h g_{Zn}^{-1} (Fig. 6c). The discharge polarization and corresponding power density profiles were presented in Fig. 6(d), Ru/HfO_2-NC achieved a peak power density of 157.3 mW cm^{-2} at 258 mA cm^{-2}, surpassing that of Pt/C (136.1 mW cm^{-2} at 170 mA cm^{-2}) and comparable with the recently reported catalysts (Fig. 6e and Table S5). In addition, the long-term rechargeability of Ru/HfO_2-NC was evaluated by galvanostatic charging-discharging at a current density of 5 mA cm^{-2} with 20 min per cycle. Significantly, the addition of RuO_2 aimed to ensure their charging capability. As shown in Fig. 6(f), the Ru/HfO_2-NC + RuO_2 exhibited a lower charge–discharge gap of

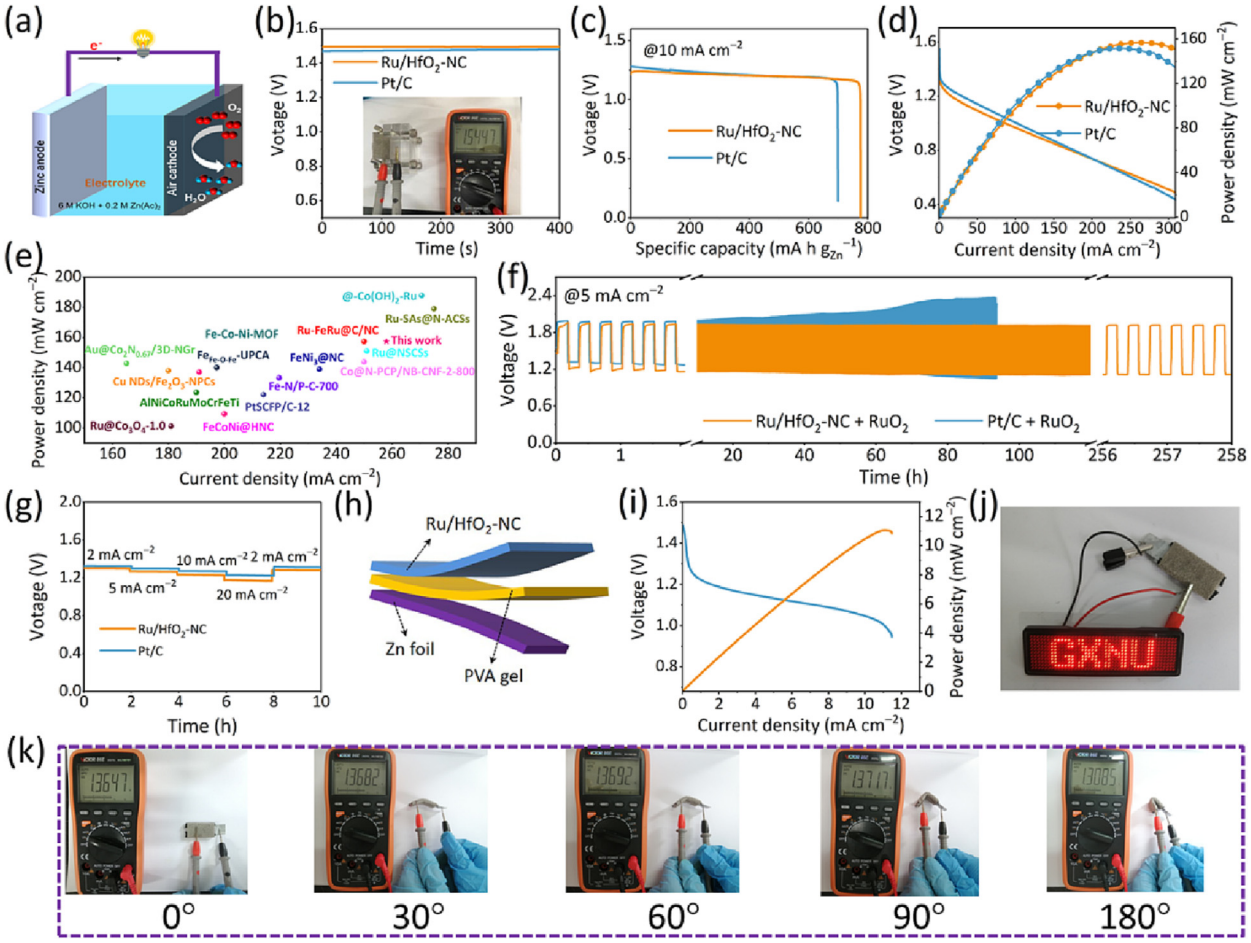

Fig. 6. (a) Sketch diagram of ZAB device. (b) Open circuit voltage (OCV) of Pt/C and Ru/HfO_2-NC based ZAB. (c) Specific capacity of Pt/C and Ru/HfO_2-NC at 10 mA cm^{-2}. (d) The discharge polarization and corresponding power density profiles. (e) Comparison of ZAB performance between Ru/HfO_2-NC and recently reported catalysts. (f) Galvanostatic charge–discharge cycling curves at a current density of 5 mA cm^{-2} (20 min per cycle). (g) Discharge plateaus of Ru/HfO_2-NC at different current densities. (h) Sketch diagram of the flexible ZAB. (i) The discharge polarization and corresponding power density profiles of Ru/HfO_2-NC-based flexible ZAB. (j) LED lighting demonstration of Ru/HfO_2-NC based flexible ZAB. (k) OCV at different bending angles.

0.83 V and steadily operated for 258 h with negligible gap increase, whereas the Pt/C + RuO_2 output a continuously increasing voltage gap. This further demonstrated its outstanding anti-polarization ability during charge/discharge process and promising application prospect in ZAB. Moreover, Ru/HfO_2-NC showed smooth voltage plateaus at different current densities, and the first voltage plateau at 2 mA cm^{-2} was 1.30 V. At the same time, the last was 1.28 V, a drop of only 1.5 %, indicating its superior rate performance (Fig. 6g). For comparison, a 1.1 % drop was observed for Pt/C.

In zinc-air batteries, after several tests, we found that the open-circuit voltage of Pt/C-based battery was close to that of Ru/HfO_2-NC-base battery, while the power density and specific capacity were less than Ru/HfO_2-NC. The discharge voltage of the Pt/C was higher than Ru/HfO_2-NC, but the stability was still poor. The results, therefore, showed that Pt/C outperforms Ru/HfO_2-NC at lower discharge current densities and was inferior to Ru/HfO_2-NC at higher current densities or more extended discharge periods. Since zinc-air batteries use a 6 M KOH solution as the electrolyte, the poor stability of Pt/C may make it more susceptible to corrosion, leading to deterioration in performance, which has been reported in the literature as well [58].

To explore the application of Ru/HfO_2-NC in flexible ZAB batteries, we assembled a solid-state battery in a sandwich-like configuration. As shown in Fig. 6(h), the flexible ZAB battery used Ru/HfO_2-NC-coated carbon cloth as the air cathode, polyvinyl alcohol (PVA) hydrogel electrolyte as the solid-electrolyte and zinc foil as the anode. Fig. 6(i) showed the discharge polarization and corresponding power density curves of the as-assembled battery, which peak power density reached 11.2 mW cm^{-2}. In addition, one assembled battery could power a LED board, proving its great discharge capacity (Fig. 6j). Moreover, we tested the OCV of the flexible battery at different bending angles to study its stability (Fig. 6k). The flexible battery exhibited a high OCV (1.36 V) and remained relatively stable at different levels of bending, demonstrating its good stability. We also studied the cycling stability of the flexible battery by performing galvanostatic charge–discharge at a current density of 5 mA cm^{-2} with 20 min per cycle. As shown in Fig. S25, Ru/HfO_2-NC + RuO_2 can continuously charge–discharge for 350 min while the stability of Pt/C + RuO_2 was 250 min under the same condition, indicating better stability as compared to the Pt/C + RuO_2 system.

4. Conclusions

In summary, a heterogeneous composite with porous nitrogen-doped carbon nested Ru/HfO_2 nanoparticles was successfully constructed and tested for alkaline ORR and ZAB. ZIF-assisted approach allowed the in-situ construction of the conductive carbon support with the intercalation of Ru and HfO_2 species to be

achieved in a facile three-step process. BET measurement demonstrated the porosity and big specific surface for Ru/HfO_2-NC. EPR and HR-TEM tests verified the presence of oxygen vacancies. DFT calculations revealed that Ru atom was the active site in Ru/HfO_2-NC, but the electronic interaction between Ru and HfO_2 reconfigured the electronic structure between them, thus modulating the *d*-band center of the catalyst. Remarkably, Ru/HfO_2-NC exhibited superior ORR activity with $E_{1/2}$ being 0.83 V in 0.1 M KOH solution, and the excellent durability may be due to the nested structure preventing the agglomeration and exfoliation of the nanoparticles. In ZAB tests, it showed a higher OCV, peak power density, specific capacity, and long-term durability. Additionally, Ru/HfO_2-NC also demonstrated a potential application in flexible ZAB. This work demonstrated the effectiveness of HfO_2-based catalyst in alkaline ORR and provided a consult for the rational design of Hf-based catalysts.

Declaration of competing interest

The authors declare that they have no known competing financial interests or personal relationships that could have appeared to influence the work reported in this paper.

Acknowledgments

This work has been supported by the National Natural Science Foundation of China (21965005), the Natural Science Foundation of Guangxi Province (2021GXNSFAA076001), the Project of High-Level Talents of Guangxi (F-KA18015), and Guangxi Technology Base and Talent Subject (GUIKE AD18126001, GUIKE AD20297039).

Appendix A. Supplementary data

Supplementary data to this article can be found online at https://doi.org/10.1016/j.jechem.2022.XX.XXX.

Supplementary data to this article can be found online at https://doi.org/10.1016/j.jechem.2023.01.047.

References

[1] Y. Zhou, Q. Wang, X. Tian, J. Chang, L. Feng, J. Energy Chem. 75 (2022) 46–54.
[2] S.L. Zhao, L.N. Ban, J.T. Zhang, W.T. Yi, W. Sun, Z.H. Zhu, Chem. Eng. J. 409 (2021).
[3] M. Shao, Q. Chang, J.-P. Dodelet, R. Chenitz, Chem. Rev. 116 (2016) 3594–3657.
[4] R. Cao, J.-S. Lee, M. Liu, J. Cho, Adv. Energy Mater. 2 (2012) 816–829.
[5] A. Sarapuu, E. Kibena-Põldsepp, M. Borghei, K. Tammeveski, J. Mater. Chem. A 6 (2018) 776–804.
[6] X.F. Lu, B.Y. Xia, S.-Q. Zang, X.W. Lou, Angew. Chem. Int. Ed. 59 (2020) 4634–4650.
[7] M.L. Pegis, C.F. Wise, D.J. Martin, J.M. Mayer, Chem. Rev. 118 (2018) 2340–2391.
[8] Y. Zhou, Y.N. Yu, D.S. Ma, A.C. Foucher, L. Xiong, J. Zhang, E.A. Stach, Q. Yue, Y.J. Kang, ACS Catal. 11 (2020) 74–81.
[9] C.Z. Zhu, H. Li, S.F. Fu, D. Du, Y.H. Lin, Chem. Soc. Rev. 45 (2016) 517–531.
[10] D. Göhl, A. Garg, P. Paciok, K.J.J. Mayrhofer, M. Heggen, Y. Shao-Horn, R.E. Dunin-Borkowski, Y. Román-Leshkov, M. Ledendecker, Nat. Mater. 19 (2020) 287–291.
[11] A. Zitolo, V. Goellner, V. Armel, M.-T. Sougrati, T. Mineva, L. Stievano, E. Fonda, F. Jaouen, Nat. Mater. 14 (2015) 937–942.
[12] G. Zhu, H. Yang, Y. Jiang, Z. Sun, X. Li, J. Yang, H. Wang, R. Zou, W. Jiang, P. Qiu, W. Luo, Adv. Sci. 9 (2022) 2200394.
[13] J. Zhang, X. Dong, W. Xing, Y. Luo, Y. Chen, Y. Xue, C. Zhang, J. Chen, G. Wang, R. Wang, Chem. Eng. J. 420 (2021).
[14] Y. Yuan, J.C. Wang, S. Adimi, H.J. Shen, T. Thomas, R.G. Ma, J.P. Attfield, M.H. Yang, Nat. Mater. 19 (2020) 282–286.
[15] C. Defilippi, D.V. Shinde, Z. Dang, L. Manna, C. Hardacre, A.J. Greer, C.D. Agostino, C. Giordano, Angew. Chem. Int. Ed. 58 (2019) 15464–15470.
[16] M. Chisaka, Y. Suzuki, T. Iijima, Y. Ishihara, R. Inada, Y. Sakurai, E.C.S. Electrochem, Lett. 1 (2012) F4–F8.
[17] M. Chisaka, N. Itagaki, Electrochim. Acta 201 (2016) 279–285.
[18] M.D. Meganathan, T. Huang, H. Fang, J. Mao, G. Sun, RSC Adv. 9 (2019) 2599–2607.
[19] M. Chisaka, Y. Suzuki, T. Iijima, Y. Sakurai, J. Phys. Chem. C 115 (2011) 20610–20617.
[20] Y. Guo, D. Wu, M. Li, K. Wang, S. Zhang, G. He, H. Yin, C. Huang, B. Yang, J. Zhang, Small Sci. 2 (2022) 2200035.
[21] Y. Zhang, T. Hu, C. Ke, F. Han, W. Xiao, X. Yang, Inorg. Chem. Front. 9 (2022) 5774–5782.
[22] M. Wei, S. Huang, Y. Wang, Y. Liu, Y. He, C. Wang, L. Yang, J. Alloys Compd. 827 (2020).
[23] D. Hu, R. Wang, P. Du, G. Li, Y. Wang, D. Fan, X. Pan, Ceram. Int. 48 (2022) 6549–6555.
[24] D.Y. Xie, D.S. Yu, Y.N. Hao, S.L. Han, G.H. Li, X.L. Wu, F. Hu, L.L. Li, H.Y. Chen, Y.F. Liao, S.J. Peng, Small 17 (2021) 2007239.
[25] M. Li, S. Wang, X. Wang, X. Tian, X. Wu, Y. Zhou, G. Hu, L. Feng, Chem. Eng. J. 442 (2022).
[26] J.J. Shi, P.F. An, H. Tian, X.X. Shu, C.S. Xiang, H. Li, Y. Li, W. Du, J.T. Zhang, H.B. Xia, J. Mater. Chem. A 9 (2021) 6861–6871.
[27] Z. Li, L. Leng, S. Ji, M. Zhang, H. Liu, J. Gao, J. Zhang, J.H. Horton, Q. Xu, J. Zhu, J. Energy Chem. 73 (2022) 469–477.
[28] J. Mao, P. Liu, J. Li, J. Yan, S. Ye, W. Song, J. Energy Chem. 73 (2022) 240–247.
[29] Y. Yang, Y. Huang, S. Zhou, Y. Liu, L. Shi, T.T. Isimjan, X. Yang, J. Energy Chem. 72 (2022) 395–404.
[30] Y. Xu, R. Wang, J. Wang, Y. Zhang, T. Jiao, J. Energy Chem. 71 (2022) 36–44.
[31] T. Lu, X. Hu, J. He, R. Li, J. Gao, Q. Lv, Z. Yang, S. Cui, C. Huang, Nano Energy 85 (2021).
[32] Y. Liu, L. Ojamae, J. Phys. Chem. A 118 (2014) 11641–11651.
[33] G. Li, H. Jang, S. Liu, Z. Li, M.G. Kim, Q. Qin, X. Liu, J. Cho, Nat. Commun. 13 (2022) 1270.
[34] Y. Lu, Y. Huang, Y. Zhang, J.-J. Cao, H. Li, C. Bian, S.C. Lee, Appl. Catal. B: Environ. 231 (2018) 357–367.
[35] G. Cui, Y. Zeng, J. Wu, Y. Guo, X. Gu, X.W. Lou, Adv. Sci. 9 (2022) 2106067.
[36] H. Zhang, P. Li, H. Zhou, J. Xu, Q. Jiang, J.H.L. Hadden, Y. Wang, M. Wang, S. Chen, F. Xie, D.J. Riley, Nano Energy 94 (2022).
[37] Z.H. Wang, H.H. Jin, T. Meng, K. Liao, W.Q. Meng, J.L. Yang, D.P. He, Y.L. Xiong, S. C. Mu, Adv. Funct. Mater. 28 (2018) 1802596.
[38] M. Guo, Z. Huang, Y. Qu, L. Wang, H. Li, T.T. Isimjan, X. Yang, Appl. Catal. B: Environ. 320 (2023).
[39] Y. Yang, X. Shao, S. Zhou, P. Yan, T.T. Isimjan, X. Yang, ChemSusChem 14 (2021) 2992–3000.
[40] F. Xiao, G.L. Xu, C.J. Sun, M.J. Xu, W. Wen, Q. Wang, M. Gu, S.Q. Zhu, Y.Y. Li, Z.D. Wei, X.Q. Pan, J.A. Wang, K. Amine, M.H. Shao, Nano Energy 61 (2019) 60–68.
[41] C. Hu, C. Gu, M. Guo, Y. Hu, J. Dong, L. D'Souza, I. Tayirjan Taylor, X. Yang, Int. J. Energy Res. 46 (2022) 12378–12390.
[42] G. Meng, H. Tian, L. Peng, Z. Ma, Y. Chen, C. Chen, Z. Chang, X. Cui, J. Shi, Nano Energy 80 (2021).
[43] H. Idriss, Surf. Sci. 712 (2021).
[44] S. Xu, Y. Kim, D. Higgins, M. Yusuf, T.F. Jaramillo, F.B. Prinz, Electrochim. Acta 255 (2017) 99–108.
[45] X. Tang, R. Cao, L. Li, B. Huang, W. Zhai, K. Yuan, Y. Chen, J. Mater. Chem. A 8 (2020) 25919–25930.
[46] R. Zhou, S.Z. Qiao, Chem. Mater. 26 (2014) 5868–5873.
[47] Y. Jiao, Y. Zheng, M. Jaroniec, S.Z. Qiao, Chem. Soc. Rev. 44 (2015) 2060–2086.
[48] X. Liang, J. Chen, B. Hong, T. Wan, W. Weng, W. Xiao, J. Energy Chem. 74 (2022) 212–217.
[49] M. Qian, M. Xu, S. Zhou, J. Tian, T. Taylor Isimjan, Z. Shi, X. Yang, J. Colloid Interface Sci. 564 (2020) 276–285.
[50] Y. Mun, S. Lee, K. Kim, S. Kim, S. Lee, J.W. Han, J. Lee, J. Am. Chem. Soc. 141 (2019) 6254–6262.
[51] C. Hu, Q. Liang, Y. Yang, Q. Peng, Z. Luo, J. Dong, T.T. Isimjan, X. Yang, J. Colloid Interface Sci. 633 (2022) 500–510.
[52] S. Dou, C. Hu, L. Shi, W. Zhang, S. Zhou, P. Yan, L. D'Souza, T.T. Isimjan, X. Yang, ChemCatChem 13 (2021) 3628–3635.
[53] X. Shao, Y. Yang, Y. Liu, P. Yan, S. Zhou, T. Taylor Isimjan, X. Yang, J. Colloid Interface Sci. 607 (2022) 826–835.
[54] J.Q. Lv, Z.L. Lang, J.Q. Fu, Q. Lan, R. Liu, H.Y. Zang, Y.G. Li, D.D. Ye, C. Streb, Angew. Chem. Int. Ed. 61 (2022) e202202650.
[55] J. Zhang, T. Wang, D. Pohl, B. Rellinghaus, R. Dong, S. Liu, X. Zhuang, X. Feng, Angew. Chem. Int. Ed. 55 (2016) 6702–6707.
[56] Y. Liu, H.T.D. Bui, A.R. Jadhav, T. Yang, S. Saqlain, Y. Luo, J. Yu, A. Kumar, H. Wang, L. Wang, V.Q. Bui, M.G. Kim, Y.D. Kim, H. Lee, Adv. Funct. Mater. 31 (2021) 2010718.
[57] Z. Wang, X. Liao, M. Zhou, F. Huang, K.A. Owusu, J. Li, Z. Lin, Q. Sun, X. Hong, C. Sun, Y.B. Cheng, Y. Zhao, L. Mai, Energy Environ. Mater. (2023), https://doi.org/10.1002/eem2.12409.
[58] W. Niu, Y. Luo, L. Wu, G. Liu, X. Du, Y. Wang, J. Li, Z. Chen, Chem. Eng. J. 442 (2022).